nature plants

Article

https://doi.org/10.1038/s41477-026-02240-9

Amazon rainforests are rejuvenating their canopies by producing more photosynthetically efficient young leaves under climate change

Received: 21 March 2025

Accepted: 29 January 2026

Xueqin Yang[1,34], Jie Tian[1,34], Philippe Ciais[2], Liming Zhou[3], Peter B. Reich[4,5], Jin Wu[6,7], Jiali Shang[8], Jérôme Chave[9], Julien Lamour[9], Isabelle Maréchaux[10], Yongshuo H. Fu[11], Jing Ming Chen[12], Jane Liu[12], Shengli Tao[13], Xiangming Xiao[14], Xiangtao Xu[15], Yongxian Su[16], Haicheng Zhang[17], Zaichun Zhu[18], Yao Zhang[19], Dalei Hao[20], Lei Chen[21], Qiang Liu[22,23], Raffaele Lafortezza[24], Kai Yan[25], Peng Li[26], Xing Li[17], Patrick Meir[27], Hui Liu[28], Damien Bonal[29], Bruce W. Nelson[30], Hao Tang[31], Jingrui Wang[1], Kailiang Yu[32], Wenping Yuan[17], Shuo Wang[33] & Xiuzhi Chen[1] ✉

Leaf age structure strongly regulates canopy photosynthesis in Amazon rainforests yet its large-scale patterns and dynamics remain poorly understood. Here we map the fraction of leaf area of photosynthetically efficient young leaves (f_{young}) using remote sensing data and assess its spatiotemporal variability from 2001 to 2023. We find that f_{young} varies markedly with elevation and canopy height: tall or mountain forests (canopy ≥32 m or elevation ≥300 m) exhibit higher f_{young} than short or lowland forests, reflecting higher leaf turnover driven by stronger radiation, greater atmospheric dryness and longer dry seasons. Across the basin, f_{young} increased significantly in 85.2% of forests during 2001–2023, linked to decreasing precipitation, rising sunlight, intensifying atmospheric dryness and lengthening dry seasons. This widespread trend towards more juvenile leaves is projected to persist under future climate change. Our findings reveal a fundamental shift in Amazon leaf age structure and highlight its importance for predicting future photosynthetic responses in a warmer, drier climate.

Leaf age is a key determinant of plant resource allocation and photosynthetic performance[1]. Older leaves generally have lower photosynthetic rates than younger, fully expanded leaves[2–5], often associated with a lower leaf nitrogen content[6,7] and older leaf functional traits[8], reflecting a shift from resource acquisition to conservation[6–9]. Consequently, as leaves age, plants frequently reallocate resources from older leaves to younger, actively growing leaves[9–11], optimizing overall photosynthetic output under changing environmental conditions by regulating canopy leaf age structure rather than maximizing the performance of individual leaves[12].

This strategy is particularly evident in the Amazon rainforests, which contribute ~34% of terrestrial gross primary production (GPP)[13]. Site-level observations, from direct leaf labelling[14] and phenological camera monitoring[1,15–17], show that dry seasons are marked by a rising proportion of young, photosynthetically efficient leaves (3–5-months old) and fewer old leaves (≥6 months)[18–23]. In essence, this seasonal shift

A full list of affiliations appears at the end of the paper. ✉e-mail: chenxzh73@mail.sysu.edu.cn

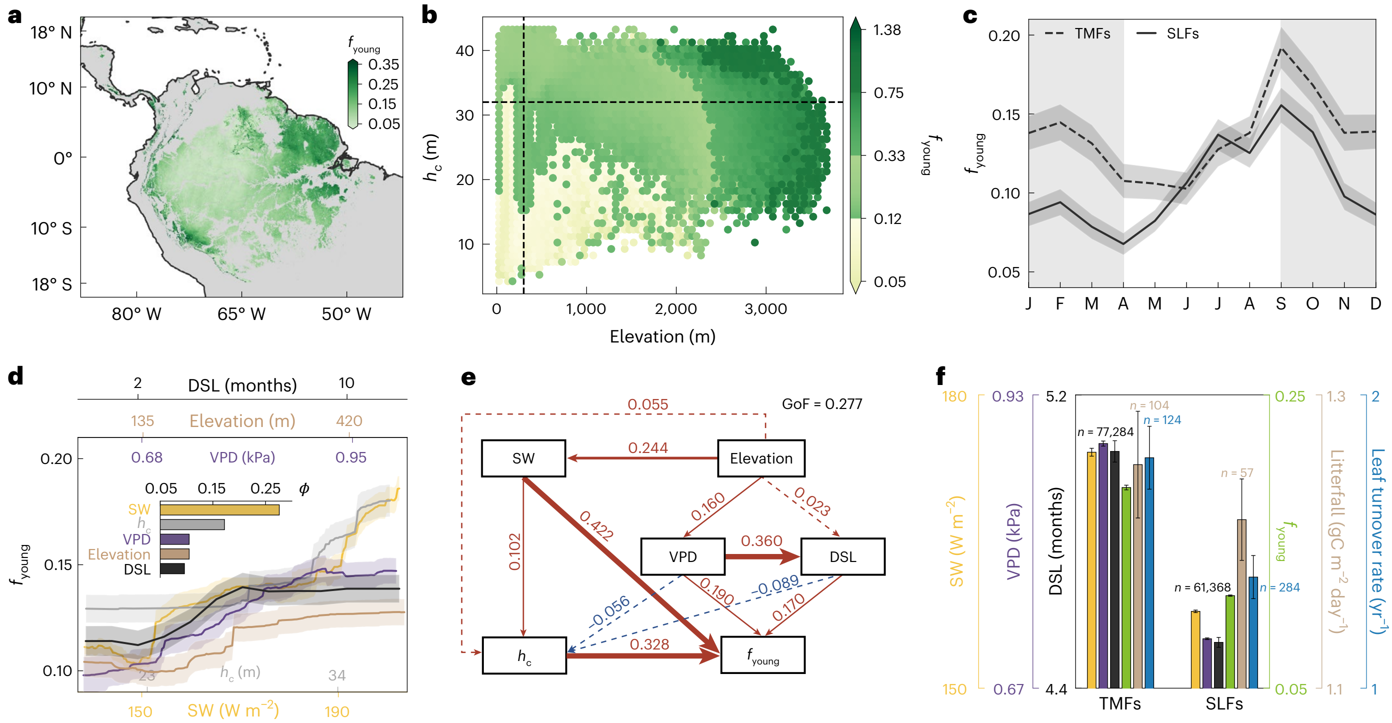

Fig. 1 | Spatial variations in satellite-inferred annual mean fraction of young, fully expanded leaves (3–5 months) (f_{young}) at 1-km resolution across Amazon rainforests. a, A map of satellite-inferred annual mean f_{young} data at a 1-km spatial resolution. **b**, The variation of satellite-inferred annual mean f_{young} against elevation (m) and h_c (m). The vertical and horizontal dashed lines indicate elevation of 300 m and h_c of 32 m, respectively. **c**, Seasonality of regionally averaged f_{young} (mean ± s.e.m.) in TMFs and SLFs, respectively. The grey backgrounds in **c** indicate the dry-to-wet transition seasons, defined as the latter half of the dry season and early half of the wet season[30]. Dry seasons were identified as months with precipitation <100 mm (ref. 114) or less than one-third of the precipitation range (0.33 × (maximum − minimum) + minimum) in cases where monthly rainfall all exceeded 100 mm year round[114–116]. The shadings in curve graphs represent one standard error. **d**, PDPs of the relationships between regional variations in satellite-inferred f_{young} and elevation, h_c, and key climate drivers (SW, VPD and DSL) (in 'Exploring environmental drivers of f_{young} using PLS-SEM and RF models' in Methods and Supplementary Fig. 5). The shadings in the curve graphs represent one standard error. The inset bars represent the average contributions (∅) of corresponding drivers to f_{young} estimated using the RF method. **e**, PLS-SEM (in 'Exploring environmental drivers of f_{young} using PLS-SEM and RF models' in Methods) depicting the impacts of elevation, h_c and key climatic drivers (that is, SW, VPD and DSL) on f_{young}. The line thickness indicates the corresponding path coefficient with the value over the line. The GoF is an indicator for assessing the overall predictive performance of the PLS-SEM. **f**, The average SW, VPD, DSL, f_{young}, litterfall and leaf turnover rate in TMFs and SLFs during the dry-to-wet seasons. The bars in the insert show the mean ± s.e.m. and *n* denotes the number of samples for each bar.

in leaf age structure is a key driver of the dry-season photosynthesis increases observed in Amazon rainforests[17,24–26] as young tropical leaves exhibit higher maximum rate of Rubisco carboxylation at 25 °C ($V_{c,max25}$) than old leaves[1,20,26,27]. Therefore, investigating the spatiotemporal variability of leaf age structure in Amazon rainforests is essential for assessing their GPP trend under climate change. Yet continental-scale patterns of leaf age structure remain poorly understood[18,28–31] due to the scarcity of in situ measurements[18,28,29], highlighting the need and urgency to explore new technologies for mapping the leaf age structure across Amazon rainforests.

To fill this knowledge gap, we developed a novel framework to reconstruct spatiotemporal variations in leaf age structure across the Amazon rainforests over the period 2001–2023. First, canopy foliage was categorized into three age cohorts: newly flushed (1–2 months), young fully expanded (3–5 months) and old (≥6 months) (in 'Defining leaf age cohorts' in Methods). Second, we mapped the fraction of young fully expanded leaf area (f_{young}) relative to total leaf area as a proxy for the three leaf age categories at 1-km resolution across the entire Amazon rainforests (~18° N–18° S) from global Penman–Monteith–Leuning Evapotranspiration V2 (PML-V2) GPP products (500-m resolution)[32] over the period 2001–2023 (method descriptions in 'Mapping satellite-based f_{young}' in Methods and Supplementary Fig. 1; validations in 'Validations of f_{young} spatially and temporally' in Methods and Supplementary Figs. 2 and 3). Third, we analysed the spatial and temporal variations in f_{young} and their environmental drivers (in 'Exploring environmental drivers of f_{young} using PLS-SEM and RF models' in Methods and Figs. 1–3). Finally, we developed random forest (RF) machine-learning (ML) models to link leaf age proxies to present-day environmental variables, ultimately projecting future f_{young} dynamics to 2100[33] using climate simulations from Coupled Model Intercomparison Project Phase 6 (CMIP6)[34] (in 'Future projections using RF-trained ML models' in Methods and Fig. 4).

Results

Spatial variations

By examining f_{young} maps against geographic variables (latitude, longitude and elevation) and plant traits (canopy height (h_c) and root depth (d_{root})) (Supplementary Fig. 4a–e), we found that f_{young} strongly depended on elevation and h_c (Fig. 1a,b). Tall or mountain forests (TMFs) (elevation ≥300 m (ref. 35) or $h_c \geq 32.0$ m (ref. 36); Supplementary Fig. 4f, green region) exhibited an overall larger mean f_{young} (0.151 ± 0.091), whereas the remaining forests (denoted as short or lowland forests (SLFs); Supplementary Fig. 4f, yellow region) had a relatively smaller mean f_{young} (0.106 ± 0.053). These differences were most pronounced during the dry-to-wet transition season[30], particularly from September to April, when f_{young} in TMFs was 1.4 times more than that in SLFs (Fig. 1c). The RF analyses (in 'Exploring environmental drivers of f_{young} using PLS-SEM and RF models' in Methods) showed that surface downwelling shortwave radiation flux (SW), vapour pressure deficit (VPD) and dry season length (DSL) were found to be the dominant climatic drivers of the TMF–SLF difference (Supplementary Fig. 5). The f_{young} increased

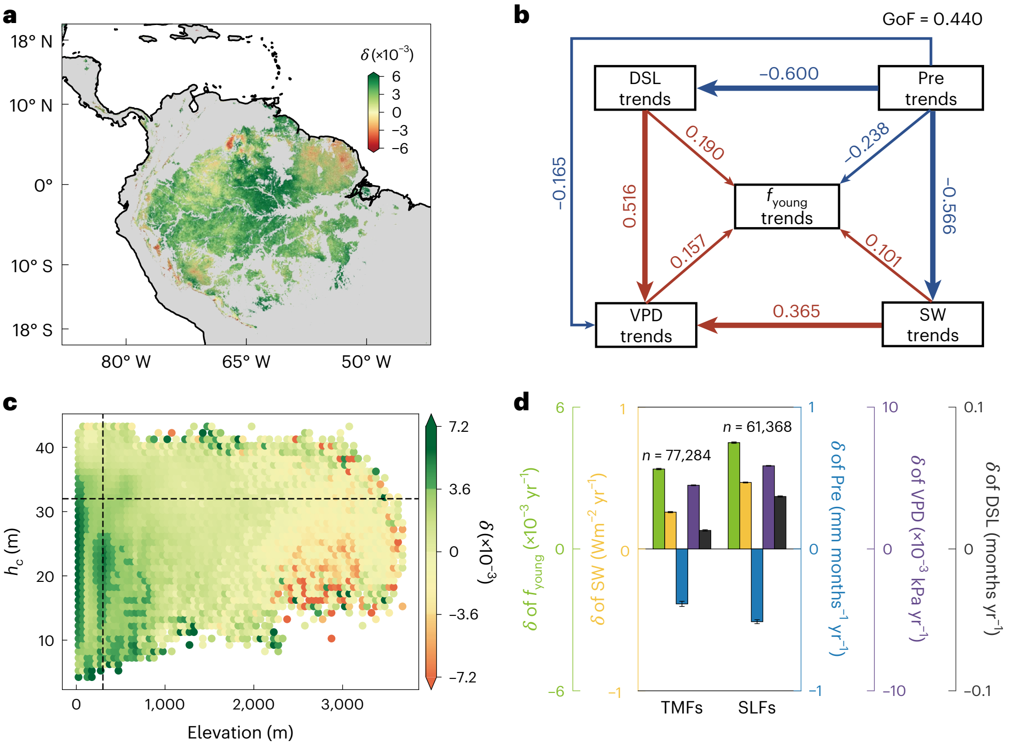

Fig. 2 | Temporal trends in satellite-inferred annual mean f_{young} across Amazon rainforests from 2001 to 2023. a, A map of the slope (δ) of the linear correlation between time-series f_{young} and the time. **b**, PLS-SEM depicting the impacts of key climatic drivers (Pre (in mm months^{-1} yr^{-1}), SW (in W m^{-2} yr^{-1}), VPD (in kPa yr^{-1}) and DSL (in months yr^{-1})) on δ of f_{young}. The line thickness represents the magnitude of the corresponding path coefficient with values given above the line. The GoF is an indicator for assessing the overall predictive performance of the PLS-SEM. **c**, Variation in δ of f_{young} against elevation (m) and h_c (m). The vertical and horizonal dashed lines indicate elevation of 300 m and h_c of 32 m, respectively. **d**, The regionally averaged slopes (δ) of the linear correlation between time-series f_{young}, SW, Pre, VPD and DSL in TMFs and SLFs. The data are shown as mean ± s.e.m. and n denotes the number of samples for each bar.

abruptly where annual mean VPD exceeded 0.72 kPa, SW was larger than 155 W m^{-2} or DSL ranged from 2.0 to 6.0 months (Fig. 1d). Partial least-squares structural equation modelling (PLS-SEM) indicated that TMFs experience higher SW (174 ± 0.19 versus 157 ± 0.15 W m^{-2}) and VPD (0.887 ± 0.001 versus 0.714 ± 0.001 kPa) and longer DSL (5.0 ± 0.016 versus 4.5 ± 0.020 months) than SLFs (Fig. 1e,f), which collectively promoted their young-leaf flushing[30] and old-leaf shedding[36]. These rejuvenating processes accelerated leaf turnover rates (Fig. 1f, blue bar) and litterfall (Fig. 1f, brown bar) in TMFs and resulted in larger f_{young} compared with SLFs (Fig. 1f, green bar).

Temporal trends

We then quantified temporal trends in f_{young} and its drivers from 2001 to 2023 using the slope (δ) of linear regressions against time. Across the majority (85.2%) of the Amazon, f_{young} exhibited a positive trend ($\delta > 0$) (Fig. 2a). The RF analyses of climatic drivers revealed that decreased precipitation (Pre) together with increased SW, VPD and DSL were the primary contributors to this younger trend in leaf age structure (Supplementary Fig. 6). Specifically, decreases in precipitation (δ of Pre = −0.441 ± 1.751 mm month^{-1} yr^{-1}, $P < 0.001$) enhanced incoming sunlight (δ of SW = 0.349 ± 0.416 W m^{-2} yr^{-1}, $P < 0.001$), extended the dry seasons (δ of DSL = 0.023 ± 0.049 months yr^{-1}, $P < 0.001$) and intensified atmospheric dryness (δ of VPD = 0.005 ± 0.003 kPa yr^{-1}, $P < 0.001$), collectively driving increases in f_{young} (Fig. 2b). The magnitude of this trend also varied with elevation and h_c (Fig. 2c). TMFs experienced moderate reductions in Pre and increases in SW, DSL and VPD, leading to a smaller δ of f_{young} (0.003 ± 0.003 yr^{-1}, $P < 0.001$), about 0.75 times lower than in surrounding SLFs (δ = 0.004 ± 0.003 yr^{-1}, $P < 0.001$), where more pronounced changes in climate drivers were observed (Fig. 2d). Notably, a small fraction of TMFs (4.1%), concentrated in the northeastern area of the region, showed a decline in f_{young} (δ = −0.0006 ± 0.0001 yr^{-1}), largely driven by shorter DSL and weaker SW (Supplementary Fig. 7).

Field-based evidence, independent validations and potential uncertainties

Potential uncertainties remain regarding the consistency between satellite and field-based observations, the robustness of leaf age–$V_{c,max25}$ thresholds over a large scale, the validity of homogeneous leaf age assumptions among adjacent forests, independent assessments of leaf age in driving GPP variability and potential uncertainties related to extreme climate events and satellite signal saturation issues.

First, the satellite-inferred f_{young} data that we obtained were validated against 341 in situ leaf lifespan data; the latter was negatively correlated with f_{young} (Supplementary Fig. 3b). The in situ leaf lifespan observations mostly suggested a trend towards shorter lifespan over their observation period (Supplementary Fig. 8a, Supplementary Data 8 and in ‘Validations of f_{young} spatially and temporally’ in Methods), consistent with an increasing trend in f_{young}. Independent species-based field evidence also supports this finding: a previous study on seven Amazonian tree species[28] reported significant reductions in leaf lifespan (Supplementary Fig. 8b), although part of that trend may have involved ontogenetic branch dynamics. We further mapped the continental-scale leaf turnover rate from seasonal dynamics of MODIS Enhanced Vegetation Index at 250-m resolution (Supplementary Fig. 9a, methods in the figure caption). Leaf turnover rate increased across >58.3% of the Amazon during 2001–2023 (Supplementary Fig. 9b), consistent with an increasing trend in f_{young}. Together, these independent validations all support a continental-scale shift towards younger canopy structures across the Amazon rainforests.

Second, the $V_{c,max25}$ thresholds of three leaf age cohorts may vary across the Amazon region and differ among species[1,3,4,24,27,37,38]. Thus,

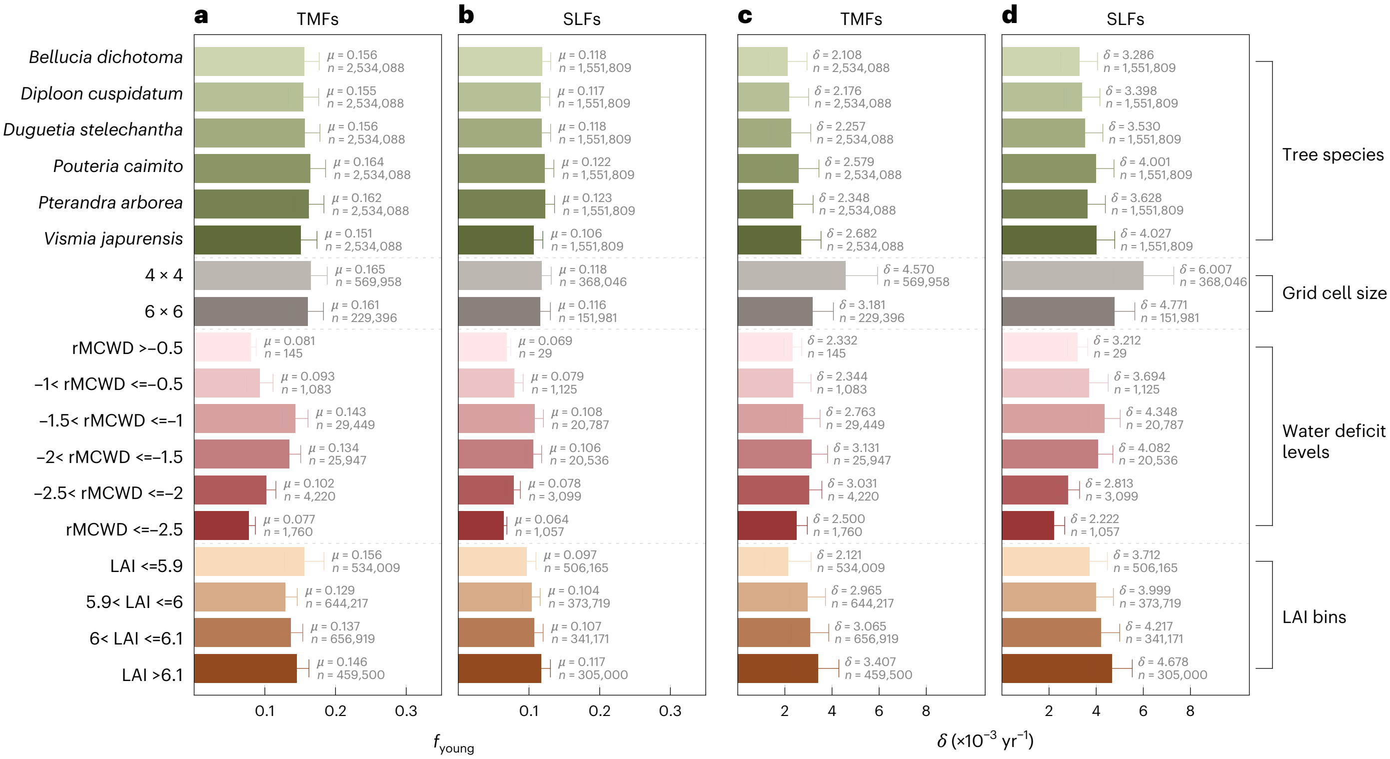

Fig. 3 | Testing potential uncertainties under different conditions. **a**,**b**, Regionally averaged f_{young} in TMFs (**a**) and SLFs (**b**) under different conditions. **c**,**d**, The δ of f_{young} in TMFs (**c**) and SLFs (**d**) under different conditions. The average f_{young} estimated based on the leaf age–$V_{c,max25}$ thresholds of six tree species are represented in green bars and the corresponding maps of f_{young} and δ are shown in Supplementary Fig. 11. The average f_{young} and δ estimated based on data of adjacent 4 × 4 and 6 × 6 grid cells in TMFs and SLFs are represented in grey bars and the corresponding maps of f_{young} and δ are shown in Supplementary Fig. 12. The average f_{young} and δ for TMFs and SLFs with different bins of rMCWD are represented in red bars. The average f_{young} and δ for TMFs and SLFs in different bins of LAI are represented in brown bars. The bars show the mean calculated from n samples, with error bars indicating ±1 s.e.m.

we matched satellite-observed $V_{c,max25}$ data[39] with continental-scale field-based leaf age measurements (Supplementary Fig. 10a). The results showed a consistent leaf age–$V_{c,max25}$ relationship over a broad spatial scale (Supplementary Fig. 10b). The f_{young} estimates using these leaf age–$V_{c,max25}$ thresholds also showed consistent spatial and temporal patterns (Supplementary Fig. 10c,d). In addition, we mapped six additional f_{young} datasets based on equation (2) using in situ leaf age–$V_{c,max25}$ thresholds of six Amazon species[14] (Supplementary Fig. 11 and in 'Defining leaf age cohorts' in Methods). These newly developed f_{young} data showed similar patterns of f_{young} between TMFs and SLFs, with their temporal trends being consistent with our findings (Fig. 3, green bars, and Supplementary Fig. 11).

Third, the assumption of a homogeneous leaf age structure among adjacent forests needs to be examined. The camera-based f_{young} at Barro Colorado and Barro Colorado2 sites in Panama, located in the same 2 × 2 500-m resolution grid cells, showed consistent seasonal cycles (Supplementary Fig. 2b). The seasonality of f_{young} at the K34 site also closely matched that of the ATTO and K67 sites, even though they were located 145 km and 583 km away, respectively (Supplementary Fig. 2b). These field-based evidences support the prevalence of rather homogeneous leaf age structures across neighbouring forests. To further test its robustness at the continental scale, we calculated the coefficient of variation of MODIS-derived leaf turnover rate within each adjacent 2 × 2 500-m resolution grid cell (Supplementary Fig. 9, see the method in figure caption). More than 89% of adjacent 2 × 2 grid cells in Amazon rainforests had coefficient of variation values below 0.4, confirming a broadly homogeneous leaf age structure among adjacent forests (Supplementary Fig. 9a). In addition, the f_{young} estimates based on adjacent 4 × 4 and 6 × 6 grid cells were all well correlated with those based on adjacent 2 × 2 grid cells (Supplementary Fig. 12), consistently supporting the robustness of our continental-scale spatial and temporal patterns (Fig. 3, grey bars).

In addition, we explored independent analyses to quantify the importance of leaf age structure dynamics in driving GPP variability in the Amazon rainforests. We applied ridge regression analysis to distinguish the strength of the contributions of f_{young} versus climate variables (VPD, SW, Ta, Pre and CO_2) to GPP, using data from the BR-Sa1 and BR-Ma2 sites (Supplementary Fig. 13a,b, see the method in the figure caption). Leaf age is shown to be the most important factor determining GPP variability. In addition, model simulations demonstrated that excluding leaf age information led to the greatest mismatch in GPP seasonality compared with the field measurements at BR-Sa1 (Kendall coefficient of −0.09) and BR-Ma2 sites (Kendall coefficient of 0.12) (Supplementary Fig. 13c,d, see the method in the figure caption), confirming leaf age as a primary driver of GPP variability in Amazon rainforests.

Finally, drought (for example, soil water deficit) is also expected to impact f_{young} significantly. To test this, we calculated relative maximum cumulative water deficit anomalies (rMCWD) following the method in ref. 40 for each pixel. We found that, across all rMCWD bins, TMFs consistently exhibited higher f_{young} than SLFs, and δ of f_{young} remained positive (Fig. 3, red bars). Notably, both f_{young} and δ of f_{young} increased under moderate water stress (rMCWD >−2.0), but declined sharply when rMCWD fell below −2.0, indicating strong suppression of severe drought on f_{young} (Fig. 3, red bars). To test robustness against potential signal saturation in dense canopies, we further stratified forests by leaf area index (LAI) (≤5.9, 5.9–6.0, 6.0–6.1 and >6.1 m^2 m^{-2}). Patterns of TMF–SLF differences and their temporal trajectories were consistent across all LAI bins (Fig. 3, brown bars).

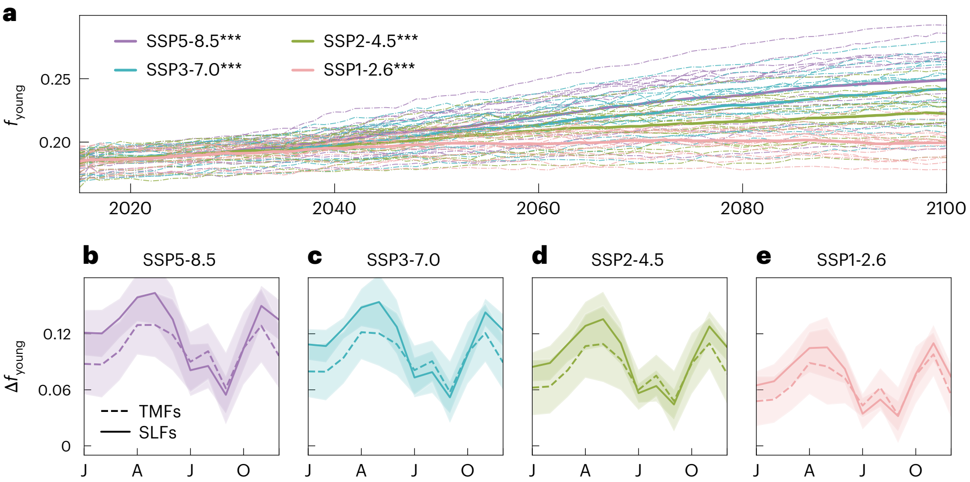

Fig. 4 | Projected future changes in annual mean f_{young} across Amazon rainforests using the well-trained ML models. a, Simulated annual mean f_{young} time series from 2015 to 2100 under different scenarios driven by the climate factors from 15 climate models (in 'Future projections using RF-trained ML models' in Methods), respectively. Each dashed curve indicates the projected result driven by the climate factors from one climate model. The purple, blue, green and red solid curves denote the multimodel ensemble mean projections under SSP5-8.5, SSP3-7.0, SSP2-4.5 and SSP1-2.6 scenarios, respectively. Asterisks indicate a significant Pearson correlation between time-series f_{young} and the time (two-sided Student's t-test, $***P < 0.001$). **b**–**e**, Seasonality of temporal changes of f_{young} (Δf_{young}) in TMFs and SLFs under different scenarios (SSP5-8.5 (**b**), SSP3-7.0 (**c**), SSP2-4.5 (**d**) and SSP1-2.6 (**e**)). Δf_{young} is calculated as the difference between two periods (the 2077–2100 average minus the 2001–2023 average). The shadings in curve graphs represents ±1 s.e.m. of the projected results driven by the climate factors from 15 climate models.

Future projections

We developed a ML model based on a RF algorithm[33] to project future trajectories of f_{young} under four distinct emission scenarios (in 'Future projections using RF-trained ML models' in Methods): high (SSP5-8.5), medium-high (SSP3-7.0), moderate (SSP2-4.5) and low (SSP1-2.6)[41]. Climatic forcing data were from 15 state-of-the-art climate models that participated in the CMIP6 project[34]. For each scenario, validations confirmed good predictive skill across 15 climate models, with RF models capturing historical trends in f_{young} ($R^2 > 0.50$) in 83.2% of grid cells (Supplementary Fig. 14a,b), with models trained on 80% of the data and validated on the remaining 20%. Additional non-random validations further affirmed model robustness (Supplementary Fig. 14c,d and in 'Future projections using RF-trained ML models' in Methods).

Under SSP5-8.5, f_{young} is projected to increase steadily ($\delta = 0.0008 \pm 0.0001\ \text{yr}^{-1}$, $P < 0.001$; Fig. 4a, purple curve) across Amazon rainforests through 2100 in a drier climate (Supplementary Fig. 15a,b,f). f_{young} shows an overall faster wet-season (January to June) increase. Specifically, SLFs experience more reductions in Pre and greater increases in SW, VPD and DSL (Supplementary Fig. 15a–g), resulting in larger Δf_{young} ($\Delta f_{\text{young}} = 0.139 \pm 0.018$) compared with TMFs ($\Delta f_{\text{young}} = 0.109 \pm 0.019$) (Fig. 4b). By contrast, both TMFs and SLFs show smaller dry-season gains ($\Delta f_{\text{young}} = 0.099 \pm 0.002$) (Fig. 4b) as climate drying intensifies future dry-season climatological water deficits (Supplementary Fig. 15h), potentially limiting the increasing magnitude of f_{young} in dry seasons.

Compared with SSP5-8.5, projected f_{young} increases more slowly under emission scenarios such as SSP3-7.0 ($\Delta f_{\text{young}} = 0.103 \pm 0.008$, $\delta = 0.0007 \pm 0.0002\ \text{yr}^{-1}$, $P < 0.001$), SSP2-4.5 ($\Delta f_{\text{young}} = 0.088 \pm 0.007$, $\delta = 0.0006 \pm 0.0001\ \text{yr}^{-1}$, $P < 0.001$) and SSP1-2.6 ($\Delta f_{\text{young}} = 0.069 \pm 0.005$, $\delta = 0.0003 \pm 0.0001\ \text{yr}^{-1}$, $P < 0.001$) (Fig. 4c–e). This gradient reflects progressively weaker growth in wet-season SW, VPD and DSL from higher to lower emission scenarios (Supplementary Fig. 15a–g). The results were consistent with projections from bias-corrected Inter-Sectoral Impact Model Intercomparison Project (ISI-MIP) climate simulations (Supplementary Fig. 16), which reduced input uncertainties by aligning modelled climate variables with observations[42].

Discussion

Large-scale shifts in leaf age structure across Amazon forests have long been overlooked owing to the lack of spatially explicit observations[30], even though leaf age is a key trait regulating GPP variability[1,26,43] (Supplementary Fig. 13). Previous studies often relied on satellite-derived vegetation indices such as Enhanced Vegetation Index and Near-Infrared Reflectance of Vegetation as proxies for young leaves over a large scale[5,44,45], but these indices do not quantify leaf age directly[46]. This limitation has been a major obstacle for simulating photosynthetic seasonality in land surface models (LSMs)[47]. Here, we derive the first continental-scale benchmark of Amazonian leaf age structure from satellite-based GPP products, offering a pathway to improve LSM representations of the tropical carbon cycle[43].

We further identified a widespread increase in photosynthetically efficient young leaves over the past two decades. This finding may challenge the prevailing view that warming and drying reduce photosynthesis in Amazon forests[33,48,49]. Instead, climate-driven shifts in leaf age structure and functional traits[12,50] suggest that photosynthesis could rise in a warmer and drier climate as greater young-leaf abundance enhances photosynthetic capacity and partly offsets stomatal limitations[50]. Longer dry seasons and elevated VPD accelerate old-leaf shedding, shorten leaf lifespan and promote canopy rejuvenation[18,50]. This strategy reallocates carbon, nitrogen and phosphorus from older to younger leaves[9,10], boosting plant carbon-use efficiency[38,51]. Our findings provide continental-scale evidence for a leaf-level optimality theory, which suggests that forests can change their leaf age structure and leaf traits to maximize whole-plant carbon gain[9], highlighting the important role of leaf age dynamics in driving GPP variability across the Amazon basin.

We also find contrasting changes in leaf age structure between TMFs and SLFs under severe droughts. TMFs, which often harbour tall canopies and low Huber values[52], experience greater hydraulic stress and stronger dry-season leaf shedding[36]. Deep rooting allows TMFs to sustain leaf flushing under mild to moderate stress[53], resulting in faster turnover and higher young-leaf fractions compared with SLFs. However, under severe droughts, TMFs show sharper declines in young-leaf fractions (Supplementary Fig. 17a,c), consistent with their greater sensitivity of canopy greenness to drought[36]. This higher vulnerability under hydraulic stress[36] can in turn reduce GPP and thus decrease the allocation of carbohydrates to canopy leaves in TMFs[52], amplifying constraints of severe droughts on flushing of young leaves. By contrast, SLFs could even increase young-leaf fraction under severe drought events (Supplementary Fig. 17b,d). This might provide explanations for previous studies that reported a 'green-up' canopy during the drought period[17,19]. Overall, intensifying drought events could curtail the rejuvenation of TMFs, whereas SLFs show larger advantages.

In summary, our study shows continental-scale heterogeneity in leaf age structure and reveals a widespread increase in the fraction of photosynthetically efficient young leaves across Amazon forests over the past decades. While the current shift towards younger canopies could enhance photosynthesis, this benefit may have limits: extreme water deficits may suppress leaf rejuvenation, bringing stronger negative impacts on photosynthesis under future climate change. Together, our findings highlight leaf age structure as a critical but overlooked regulator of Amazonian GPP. Incorporating these dynamics into LSMs is essential for predicting tropical carbon–climate feedback.

Methods

Selection of Amazon rainforest grid cells

We focused on intact Amazon rainforest areas (18° N–18° S) unaffected by anthropogenic or natural disturbances during the study period. First, 500-m grid cells classified as 'evergreen broadleaf forests' were identified using MODIS land cover imagery (MCD12Q1), and only areas with forest cover >90% were retained[54]. These grid cells were then resampled to 1-km resolution for subsequent analyses. Next, 30-m global tree cover change maps from Global Forest Watch[55] were overlaid on the 500-m MODIS land cover maps. Grid cells at 1-km resolution that had experienced forest gain or loss were excluded, following the method in ref. 56. To minimize wildfire impacts, grid cells containing burned areas were also removed. Burned areas were derived from the MODIS Fire_cci Burned Area Pixel Product (version 5.1) at 250-m spatial and monthly temporal resolution[57]. Degraded areas were further identified and excluded based on TMF forest cover change data[58].

Defining leaf age cohorts

Several studies have decomposed canopy leaves into distinct age cohorts to simulate site-level GPP in Amazon rainforests[1,27,31]. Canopy leaves have been classified into three cohorts—newly flushed (1–2 months), young, fully developed (3–5 months) and old (≥6 months)—and leaves aged 3–5 months were found to largely control seasonal GPP variation[1]. This classification was supported by ref. 27, where in situ measurements indicated that $V_{\mathrm{c,max25}}$ was highest in young, fully developed leaves, and lower in both old and newly flushed leaves.

Here we applied the aforementioned thresholds to classify Amazon leaves into newly flushed (1–2 months), young (3–5 months) and old (≥6 months) cohorts (Supplementary Fig. 1). Using 116 samples of in situ measurements of leaf age and corresponding $V_{\mathrm{c,max25}}$ data at three sites from refs. 1,14,27,38, we calculated the average $V_{\mathrm{c,max25}}$ values of each cohort (Supplementary Data 1). These values were then used to calculate photosynthetic rate per unit leaf area for deriving the LAI of newly flushed ($\mathrm{LAI}_{\mathrm{new}}$); young, fully developed ($\mathrm{LAI}_{\mathrm{young}}$); and old ($\mathrm{LAI}_{\mathrm{old}}$) leaves from GPP variable via equations (1) and (2) (Supplementary Fig. 1 and in 'Mapping satellite-based f_{young}' in Methods).

To validate the $V_{\mathrm{c,max25}}$ thresholds of three leaf age cohorts at large scales, we matched 35 field-based leaf age samples (Supplementary Fig. 10a and Supplementary Data 2) with satellite-derived $V_{\mathrm{c,max25}}$ from Global Ozone Monitoring Experiment-2 (GOME-2) Solar-Induced Fluorescence[39]. The resulting $V_{\mathrm{c,max25}}$ thresholds for new, young and old leaf age cohorts across the Amazon is shown in Supplementary Fig. 10b, with corresponding maps of f_{young} and δ in Supplementary Fig. 10c,d. We further tested robustness using alternative leaf age–$V_{\mathrm{c,max25}}$ thresholds from six Amazon species[14] (Supplementary Data 3). Corresponding f_{young} and δ maps showed the same spatial patterns (Supplementary Fig. 11).

Mapping satellite-based f_{young}

The derivation of continental-scale f_{young} from satellite-based GPP product was based on inverting a process-based model—the Farquhar–von Caemmerer–Berry (FvCB) model[59,60]—a standard framework for simulating leaf-scale photosynthesis through photosynthesis–stomatal coupling from climate data. It underpins many satellite-based and process-based modelled global GPP estimates, including the BEPS model[61,62], the P-model[63] and the Community Land Model[64]. According to the FvCB framework, GPP can be expressed as the sum of the product of LAI and gross photosynthesis per unit leaf area (gpp) when canopy leaves are grouped into different cohorts according to a certain criterion[65,66]

$$\mathrm{GPP} = \mathrm{LAI}_1 \times \mathrm{gpp}_1 + \mathrm{LAI}_2 \times \mathrm{gpp}_2 + \ldots + \mathrm{LAI}_i \times \mathrm{gpp}_i, \tag{1}$$

where LAI_i is the LAI of cohort i and gpp_i is the photosynthetic rate per unit leaf area for that cohort.

Given the demonstrated role of leaf age in regulating GPP dynamics in Amazon rainforests[31] (Supplementary Fig. 13), we partitioned the canopy leaves of Amazon rainforests into three age cohorts following established criteria[1,2,14,27]: newly flushed (1–2 months), young fully developed (3–5 months) and old (≥6 months) (Supplementary Fig. 1). Accordingly, GPP can be written as equation (2) following ref. 67

$$\mathrm{GPP} = \mathrm{LAI}_{\mathrm{new}} \times \mathrm{gpp}_{\mathrm{new}} + \mathrm{LAI}_{\mathrm{young}} \times \mathrm{gpp}_{\mathrm{young}} + \mathrm{LAI}_{\mathrm{old}} \times \mathrm{gpp}_{\mathrm{old}}, \tag{2}$$

where $\mathrm{LAI}_{\mathrm{new}}$, $\mathrm{LAI}_{\mathrm{young}}$ and $\mathrm{LAI}_{\mathrm{old}}$ represent the cohort-specific LAI, and $\mathrm{gpp}_{\mathrm{new}}$, $\mathrm{gpp}_{\mathrm{young}}$ and $\mathrm{gpp}_{\mathrm{old}}$ are the corresponding average gross primary production per leaf area.

In equation (2), GPP (left-hand side) was set using the PML-V2 GPP product (2001–2023, 500-m resolution)[32]. The gpp terms (right-hand side) were calculated as the minimum of Rubisco limitation (Wc), RuBP regeneration (Wj) and triose phosphate utilization (Wp) using the FvCB photosynthesis model[59,60] coupled with the Unified Stomatal Optimization approach[38,68], where Wc, Wj and Wp are functions of climatic drivers (that is, the incident sunlight (SW), air temperature (T_{mean}) and VPD) and $V_{\mathrm{c,max25}}$[60,69] (refer to Supplementary Fig. 1 for more details). Cohort-specific $V_{\mathrm{c,max25}}$ values were derived by averaging 116 samples of in situ measurements from the K67 site (2.86° S, 54.96° W)[1,27], the K34 site (2.61° S, 60.21° W)[38] and another site (2.58° S, 60.21° W) from ref. 14 (inset box plots in Supplementary Fig. 1 and Supplementary Data 1). Thus, $\mathrm{gpp}_{\mathrm{new}}$, $\mathrm{gpp}_{\mathrm{young}}$ and $\mathrm{gpp}_{\mathrm{old}}$ were estimated from cohort-specific $V_{\mathrm{c,max25}}$ and concurrent climate conditions. In other words, the $\mathrm{LAI}_{\mathrm{new}}$, $\mathrm{LAI}_{\mathrm{young}}$ and $\mathrm{LAI}_{\mathrm{old}}$ values derived from equation (2) inherently incorporate the effects of climate variability and therefore represent the real-word leaf age structure dynamics.

To simultaneously solve the three unknowns ($\mathrm{LAI}_{\mathrm{new}}$, $\mathrm{LAI}_{\mathrm{young}}$ and $\mathrm{LAI}_{\mathrm{old}}$) in equation (2), we assumed that groups of 2 × 2 adjacent pixels (500-m resolution) shared a homogeneous leaf age structure with similar seasonality of $\mathrm{LAI}_{\mathrm{new}}$, $\mathrm{LAI}_{\mathrm{young}}$ and $\mathrm{LAI}_{\mathrm{old}}$ (see the independent verification in 'Field-based evidence, independent validations and potential uncertainties' section). This assumption yielded four equations with three unknowns ($\mathrm{LAI}_{\mathrm{new}}$, $\mathrm{LAI}_{\mathrm{young}}$ and $\mathrm{LAI}_{\mathrm{old}}$) per 2 × 2 group (for details, refer to Supplementary Fig. 1). Then, we employed a linear least-squares solver with bounds or linear constraints (the Lsqlin function in MATLAB)[70] to search for the optimal $\mathrm{LAI}_{\mathrm{new}}$, $\mathrm{LAI}_{\mathrm{young}}$ and $\mathrm{LAI}_{\mathrm{old}}$ based on equation (2). To evaluate robustness, we repeated the procedure using 4 × 4 and 6 × 6 adjacent grid cells. The results showed highly consistent spatial and temporal patterns (Supplementary Fig. 12).

Validations of f_{young} spatially and temporally

Camera-based observations of leaf age structure for spatial validation. Leaf age-dependent seasonality of LAI can be well documented at the site level using canopy phenology cameras[1,17,27,71], which capture top-of-canopy RGB images and allow the detection of leaf age cohorts from spectral differences in the green band[12]. We restricted analysis to one geometrically adjusted image per day acquired under diffuse light—either cloudy conditions or overcast sky—to minimize illumination effects. For each crown, an abrupt increase in greenness signalled leaf emergence. The date of this event was recorded and the subsequent leaf age was calculated. Time-series daily leaf age data were then constructed by counting the number of newly flushed leaves for each month. These records were used to build a training dataset linking leaf age with brightness values. A supervised classification scheme was applied to each RGB image to separate leaves into three cohorts: new flushed (1–2 months), young (3–5 months) and old (≥6 months).

In total, we collected camera-based images from eight Amazonian sites to develop the field dataset of $\mathrm{LAI}_{\mathrm{new}}$, $\mathrm{LAI}_{\mathrm{young}}$ and $\mathrm{LAI}_{\mathrm{old}}$ (Supplementary Fig. 2a and Supplementary Data 4). Data for the K67 and K34 flux tower sites were derived from ref. 1. For the remaining six sites, we used the classification procedure described above to compute the $\mathrm{LAI}_{\mathrm{new}}$, $\mathrm{LAI}_{\mathrm{young}}$ and $\mathrm{LAI}_{\mathrm{old}}$. The camera-based canopy photos at Barro Colorado (March 2013 to December 2023), Barro Colorado2 (November 2014 to September 2015), Elverde (November 2014 to December 2020), NEON GUAN (December 2016 to September 2018) and Soltis (July 2018 to April 2022) sites were obtained from the following website[72]: https://phenocam.nau.edu/webcam/ (last access 2 October 2025). The data from the ATTO (July 2013 to November 2018) site were from ref. 15 with the data available at ref. 73 (last access 2 October 2025). Overall, our satellite-based estimates showed good agreements with these site-level camera-based $\mathrm{LAI}_{\mathrm{new}}$, $\mathrm{LAI}_{\mathrm{young}}$ and $\mathrm{LAI}_{\mathrm{old}}$ data across the eight sites (Supplementary Fig. 2).

Field-based observations of leaf lifespan for spatial validation. The satellite-derived f_{young}, calculated as the fraction of $\mathrm{LAI}_{\mathrm{young}}$ to $\mathrm{LAI}_{\mathrm{total}}$, was verified against three datasets: 10 annual mean leaf lifespan measured at 5 field sites (triangle symbols), 331 leaf lifespan estimates derived from 193 in situ leaf mass per area (LMA) records collected at 148 sites (circle symbols) and 138 litterfall seasonality records from 66 sites (square symbols) (Supplementary Fig. 3a and Supplementary Data 5–7). Ground-based leaf lifespan measurements were obtained from refs. 38,74–79 and the Plant Trait Database (TRY)[80], a global repository containing over 2.88 million trait entries across 69,000 species. All LMA data across the Amazon were collected from the TRY database[80]. Numerous studies have reported a positive linear relationship between $\log_{10}$ (LMA; in g m^{-2}) and $\log_{10}$ (LL; in days) (equation (3))[38,51,81]

$$\log_{10}(\mathrm{LL}) = \log_{10}(\mathrm{LMA}) + b, \tag{3}$$

where b is a parameter to calibrate the overall simulation accuracy. It was set to 0.90 according to LMA and LL data observed across TMFs from previous studies. Litterfall seasonality data were taken from refs. 30,82. Leaf turnover rates[83] were calculated as the ratio of (maximal litterfall − minimal litterfall) to minimal litterfall, with the reciprocal providing LL estimates.

Overall, by dividing the Amazon region into 2° × 2° grid cells, more than 31.4% of the Amazon region had field data available for validations (Supplementary Fig. 3a). Satellite-derived f_{young} agreed well with field-based lifespan estimates ($R^2 = 0.55$; 91.61% of validations within the 95% prediction interval) (Supplementary Fig. 3b).

Field-based observations for temporal validation. Long-term field-based observations of leaf age are lacking at large spatial scales[67], precluding site-level validation of temporal dynamics. Instead, we used in situ leaf age measurements collected in different years at different sites (Supplementary Fig. 3), a common approach for large-scale temporal validation[81]. These comparisons showed that our satellite-based f_{young} data reproduced interannual variations in leaf age, supporting its robustness in capturing both spatial and temporal patterns (Supplementary Fig. 3).

As there is lacking of long-term validation for each site, we thus compiled the leaf lifespan records derived from LMA and litterfall data within each 2° × 2° grid cell across the Amazon region (Supplementary Data 8). For those 2° × 2° grid cells that had lifespan data observed for at least two time points (interval ≥2 years), we quantified their lifespan changes between the last and first observation time points. The results indicated a widespread decline in lifespan across at most sites across the Amazon (Supplementary Fig. 8a), consistent with a shift towards younger canopies. Time-series lifespan records from seven Amazonian tree species[28] also revealed significant decreases from 1982 to 1989 (Supplementary Fig. 8b and Supplementary Data 9). Given the negative correlation between leaf lifespan and leaf age, these reductions in lifespan provide independent support for the observed increase trend in f_{young} across Amazon rainforests.

Exploring environmental drivers of f_{young} using PLS-SEM and RF models

We assessed the impacts of key climate variables on spatial and temporal variations in f_{young}, including atmospheric carbon dioxide concentration ($\mathrm{CO_2}$), air temperature (T_{mean}), SW, Pre, SM, VPD and DSL. Elevation and h_{c} were also included. These variables were known to regulate ecological processes across the Amazon rainforests, including leaf phenology[17,84], leaf traits[7,81], carbon and water cycles[66,85–87] and tree mortality[88–90].

RF analysis of environmental drivers of f_{young}. We applied a RF algorithm[33] to identify key climatic controls on f_{young}. RF incorporates the basic form of the Classification and Regression Tree (CART) algorithm into each tree and functions as an ensemble of decision trees, typically trained using the bagging method to enhance reliability and accuracy in predictions[91]. CART yields a significant outcome in the form of variable importance measures (VIM), a method that assesses and ranks independent variables according to their impact on the target variable[1]. The partial dependence plot (PDP)[92] is a visualization tool generated by the RF-trained ML model to show the ranking results. In this study, the CART and PDP analyses were implemented from the Partial Dependence Display module of the scikit-learn package in Python (https://scikit-learn.org/stable, last accessed 1 October 2025).

For the spatial analysis, we trained RF models with annual mean f_{young} per pixel as the response and climatic variables as predictors. VIM values derived from the CART algorithm were used to assess the relative importance ($\varnothing$) of each variable (Supplementary Fig. 5a) and PDPs were generated to illustrate relationships between f_{young} and individual drivers (Supplementary Fig. 5b–j).

For temporal analyses, we trained RF models using the long-term trends (δ) of f_{young} and climate variables. VIMs quantified the contributions of climate trends to f_{young} variability (Supplementary Fig. 6a), while PDPs depicted correlations between temporal changes in f_{young} and individual drivers (Supplementary Fig. 6b–h).

PLS-SEM analysis to unravel the pathways through which key factors influence f_{young}. We applied PLS-SEM to examine the maximum likelihood cause–effect pathway through which environmental drivers influence f_{young} (ref. 93). Based on the RF-derived ranking, we selected elevation and h_{c} as exogenous variables and incorporated the top climatic predictors (SW, VPD and DSL) as intermediate variables (Fig. 1e). Path coefficients were estimated using bootstrap resampling (2,000 iterations) and model accuracy was assessed by the Goodness of Fit (GoF) index.

Future projections using RF-trained ML models

The CMIP6 provides future climate projections based on four SSPs: high-emissions (SSP5-8.5), medium-to-high-emissions (SSP3-7.0), moderate-emissions (SSP2-4.5) and low-emissions (SSP1-2.6)[41]. In this study, we opted to use historical climate data (2001–2014) sourced from

15 CMIP6 climate models (ACCESS-ESM1-5[94], CanESM5[95], CMCC-ESM2[96], CNRM-CM6-1[97], CNRM-CM6-1-HR[98], CNRM-ESM2-1[99], GFDL-ESM4[100], GISS-E2-1-H[101], INM-CM4-8[102], INM-CM5-0[103], IPSL-CM6A-LR[104], MIROC-ES2L[105], MPI-ESM1-2-HR[106], MRI-ESM2-0[107] and UKESM1-0-LL[108]) to train the RF-based ML model for projecting future changes in LAI of different leaf age cohorts from 2015 to 2100. Presently, only three climate models, that is, CNRM-ESM2-1, GFDL-ESM4 and MRI-ESM2-0, within the CMIP6 project framework, have provided data for the seven designated climate variables: CO_2, Pre, SW, T_{mean}, VPD, SM and DSL. However, the remaining 12 climate models did not generate output for the CO_2 variable. Consequently, for future simulations involving data from these 12 climate models, we used the average value of CO_2 output from CNRM-ESM2-1, GFDL-ESM4 and MRI-ESM2-0.

The ISI-MIP, is a collaborative initiative focused on synthesizing impact projections across sectors such as agriculture, water, biome, health and infrastructure under varying global warming scenarios[42]. The ISI-MIP3b version is renowned for its bias-corrected climate data, which corrected systematic biases in simulated historical climatic data to align more closely with observations and provide a reliable foundation for nuanced climate impact analyses[109]. Therefore, here we additionally used five independent bias-corrected climate datasets of GFDL-ESM4, IPSL-CM6A-LR, MPI-ESM1-2-HR, MRI-ESM2-0 and UKESM1-0-LL models from ISI-MIP[110] to train the RF-based ML model for projecting future changes in LAI for different leaf age cohorts from 2015 to 2100, to test the robustness of future projections.

Using the historical climate data sourced from 15 CMIP6 models and five bias-corrected ISI-MIP3b models, we projected future changes in LAI for different leaf age cohorts from 2015 to 2100. Specifically, to develop the RF-based ML model, we first partitioned the entire Amazon rainforests region into 263 grid cells, each comprising a 180 × 180 arrangement of adjacent 1-km pixels. Subsequently, we used the RF algorithm to train the ML models for each grid cell and ultimately established 263 RF-trained ML models for the entire Amazon rainforests. In our investigation, 80% of LAI age cohorts were randomly selected as the training dataset, while the remaining 20% were reserved for validation. Overall, more than 83.2% of the grid cells exhibited robust linear correlations ($R^2 > 0.50$) between satellite-derived and RF-simulated f_{young}, forced by climate variables from the 15 climate models (Supplementary Fig. 14a,b). These models were also examined using alternative non-random validations to mitigate the temporal autocorrelation effects that could inflate model performance assessed under random validations[86,87,111]. We divided the 2001–2014 period into non-overlapping periods: 2001–2004, 2005–2010 and 2011–2014. Data from two of these three intervals were used for training models, while the data from the remaining interval were reserved for validations. On average, more than 37.4% of the grid cells exhibited robust linear correlations ($R^2 > 0.50$) between satellite-derived and RF-simulated f_{young} (Supplementary Fig. 14c,d).

Reporting summary

Further information on research design is available in the Nature Portfolio Reporting Summary linked to this article.

Data availability

All the original datasets used in this research are publicly available from their sources. The LAI age cohort product is available via Zenodo at https://doi.org/10.5281/zenodo.18271110 (ref. 112); PML-V2 GPP datasets from https://developers.google.com/earth-engine/datasets/catalog/CAS_IGSNRR_PML_V2_v018#description; Terraclimate T_{min}, T_{max}, Pre, VPD, SW, PET, AET and PDSI from https://www.climatologylab.org/terraclimate.html; ERA5-Land SM from https://cds.climate.copernicus.eu/cdsapp#!/dataset/reanalysis-era5-land-monthly-means?tab=overview; Global canopy height map for 2020 (h_c) from https://doi.org/10.3929/ethz-b-000609802; Global elevation from https://www.eorc.jaxa.jp/ALOS/en/dataset/aw3d30/aw3d30_e.htm; CMIP6 models variable from https://aims2.llnl.gov/search/?project=CMIP6/; ISI-MIP models from https://www.isimip.org/outputdata/?simulation_round=ISIMIP3b; MCD12Q1 v061 land cover from https://www.earthdata.nasa.gov/data/catalog/lpcloud-mcd12q1-061; Global Land Cover and Land Use Change, 2000–2020 from https://glad.umd.edu/dataset/GLCLUC2020/; ESA CCI Fire v5.1 from https://doi.org/10.5285/58f00d8814064b79a0c49662ad3af537; SPEI from https://doi.org/10.5285/ac43da11867243a1bb414e1637802dec; tropical moist forests product from https://forobs.jrc.ec.europa.eu/TMF/; camera-based time-series and seasonal LAI age cohort data from https://phenocam.nau.edu/webcam/ and https://doi.org/10.17871/ATTO.230.4.842; in situ leaf turnover rate observation data from https://doi.org/10.1016/j.baae.2016.01.006; and field LMA datasets in the Plant Trait Database (TRY) from https://www.try-db.org/TryWeb/Home.php.

Code availability

The codes used for data analysis are available via Zenodo at https://doi.org/10.5281/zenodo.18269018 (ref. 113).

References

1. Wu, J. et al. Leaf development and demography explain photosynthetic seasonality in Amazon evergreen forests. *Science* **351**, 972–976 (2016).
2. Chavana-Bryant, C. et al. Leaf age effects on the spectral predictability of leaf traits in Amazonian canopy trees. *Sci. Total Environ.* **666**, 1301–1315 (2019).
3. Niinemets, Ü, Cescatti, A., Rodeghiero, M. & Tosens, T. Leaf internal diffusion conductance limits photosynthesis more strongly in older leaves of Mediterranean evergreen broad-leaved species. *Plant Cell Environ.* **28**, 1552–1566 (2005).
4. Sobrado, M. A. Leaf age effects on photosynthetic rate, transpiration rate and nitrogen content in a tropical dry forest. *Physiol. Plant.* **90**, 210–215 (1994).
5. De Moura, Y. M. et al. Spectral analysis of amazon canopy phenology during the dry season using a tower hyperspectral camera and modis observations. *ISPRS J. Photogramm. Remote Sens.* **131**, 52–64 (2017).
6. Meir, P. et al. Acclimation of photosynthetic capacity to irradiance in tree canopies in relation to leaf nitrogen concentration and leaf mass per unit area. *Plant Cell Environ.* **25**, 343–357 (2002).
7. Aguirre-Gutiérrez, J. et al. Canopy functional trait variation across Earth's tropical forests. *Nature* **641**, 129–136 (2025).
8. Niinemets, Ü Leaf age dependent changes in within-canopy variation in leaf functional traits: a meta-analysis. *J. Plant Res.* **129**, 313–338 (2016).
9. Reich, P. B. et al. Controls on declining carbon balance with leaf age among 10 woody species in Australian woodland: do leaves have zero daily net carbon balances when they die?. *New Phytol.* **183**, 153–166 (2009).
10. Field, C. & Mooney, H. A. Leaf age and seasonal effects on light, water, and nitrogen use efficiency in a California shrub. *Oecologia* **56**, 348–355 (1983).
11. Niinemets, Ü Photosynthesis and resource distribution through plant canopies. *Plant Cell Environ.* **30**, 1052–1071 (2007).
12. Wang, H. et al. Leaf economics fundamentals explained by optimality principles. *Sci. Adv.* **9**, eadd5667 (2023).
13. Beer, C. et al. Terrestrial gross carbon dioxide uptake: global distribution and covariation with climate. *Science* **329**, 834–838 (2010).
14. Menezes, J. et al. Changes in leaf functional traits with leaf age: when do leaves decrease their photosynthetic capacity in Amazonian trees?. *Tree Physiol.* **42**, 922–938 (2022).
15. Botía, S. et al. The CO_2 record at the Amazon Tall Tower Observatory: a new opportunity to study processes on seasonal and inter-annual scales. *Glob. Change Biol.* **28**, 588–611 (2022).

16. Song, G. et al. Monitoring leaf phenology in moist tropical forests by applying a superpixel-based deep learning method to time-series images of tree canopies. *ISPRS J. Photogramm. Remote Sens.* **183**, 19–33 (2022).
17. Lopes, A. P. et al. Leaf flush drives dry season green-up of the Central Amazon. *Remote Sens. Environ.* **182**, 90–98 (2016).
18. Saleska, S. R. et al. Dry-season greening of Amazon forests. *Nature* **531**, E4–E5 (2016).
19. Huete, A. R. et al. Amazon rainforests green-up with sunlight in dry season. *Geophys. Res. Lett.* **33**, L06405 (2006).
20. Doughty, C. E. & Goulden, M. L. Seasonal patterns of tropical forest leaf area index and CO_2 exchange. *J. Geophys. Res. Biogeosci.* **113**, G00B06 (2008).
21. Brando, P. M. et al. Seasonal and interannual variability of climate and vegetation indices across the Amazon. *Proc. Natl Acad. Sci. USA* **107**, 14685–14690 (2010).
22. Detto, M. et al. Resource acquisition and reproductive strategies of tropical forest in response to the El Niño–Southern Oscillation. *Nat. Commun.* **9**, 913 (2018).
23. Wang, S. et al. Estimation of leaf photosynthetic capacity from leaf chlorophyll content and leaf age in a subtropical evergreen coniferous plantation. *J. Geophys. Res. Biogeosci.* **125**, e2019JG005020 (2020).
24. Xue, M. et al. Pantropical moist forests are converging towards a middle leaf longevity. *Nat Commun.* https://doi.org/10.1038/s41467-026-68989-x (2026)
25. Myneni, R. B. et al. Large seasonal swings in leaf area of Amazon rainforests. *Proc. Natl Acad. Sci. USA* **104**, 4820–4823 (2007).
26. De Weirdt, M. et al. Seasonal leaf dynamics for tropical evergreen forests in a process-based global ecosystem model. *Geosci. Model Dev.* **5**, 1091–1108 (2012).
27. Albert, L. P. et al. Age-dependent leaf physiology and consequences for crown-scale carbon uptake during the dry season in an Amazon evergreen forest. *New Phytol.* **219**, 870–884 (2018).
28. Reich, P. B. et al. Leaf demography and phenology in Amazonian rain forest: a census of 40,000 leaves of 23 tree species. *Ecol. Monogr.* **74**, 3–23 (2004).
29. Albert, L. P. et al. Cryptic phenology in plants: case studies, implications, and recommendations. *Glob. Change Biol.* **25**, 3591–3608 (2019).
30. Yang, X. et al. A comprehensive framework for seasonal controls of leaf abscission and productivity in evergreen broadleaved tropical and subtropical forests. *Innovation* **2**, 100154 (2021).
31. Chen, X. et al. Novel representation of leaf phenology improves simulation of Amazonian evergreen forest photosynthesis in a land surface model. *J. Adv. Model. Earth Syst.* **12**, e2018MS001565 (2020).
32. Zhang, Y. et al. Coupled estimation of 500 m and 8-day resolution global evapotranspiration and gross primary production in 2002–2017. *Remote Sens. Environ.* **222**, 165–182 (2019).
33. Yang, H. et al. Climatic and biotic factors influencing regional declines and recovery of tropical forest biomass from the 2015/16 El Niño. *Proc. Natl Acad. Sci. USA* **119**, e2101388119 (2022).
34. Eyring, V. et al. Overview of the coupled model intercomparison project phase 6 (CMIP6) experimental design and organization. *Geosci. Model Dev.* **9**, 1937–1958 (2016).
35. Kapos, V. et al. in *Forests in Sustainable Mountain Development: A State of Knowledge Report for 2000. Task Force on Forests in Sustainable Mountain Development* https://doi.org/10.1079/9780851994468.0004 (CABI, 2000).
36. Liu, L. et al. Tropical tall forests are more sensitive and vulnerable to drought than short forests. *Glob. Change Biol.* **28**, 1583–1595 (2022).
37. Han, Q. et al. Leaf-age effects on seasonal variability in photosynthetic parameters and its relationships with leaf mass per area and leaf nitrogen concentration within a *Pinus densiflora* crown. *Tree Physiol.* **28**, 551–558 (2008).
38. Xu, X. et al. Variations of leaf longevity in tropical moist forests predicted by a trait-driven carbon optimality model. *Ecol. Lett.* **20**, 1097–1106 (2017).
39. Chen, J. M. et al. Global datasets of leaf photosynthetic capacity for ecological and earth system research. *Earth Syst. Sci. Data* **14**, 4077–4093 (2022).
40. Papastefanou, P. et al. Recent extreme drought events in the Amazon rainforest: assessment of different precipitation and evapotranspiration datasets and drought indicators. *Biogeosciences* **19**, 3843–3861 (2022).
41. O'Neill, B. C. et al. The Scenario Model Intercomparison Project (ScenarioMIP) for CMIP6. *Geosci. Model Dev.* **9**, 3461–3482 (2016).
42. Warszawski, L. et al. The Inter-Sectoral Impact Model Intercomparison Project (ISI–MIP): project framework. *Proc. Natl Acad. Sci. USA* **111**, 3228–3232 (2014).
43. Restrepo-Coupe, N. et al. Do dynamic global vegetation models capture the seasonality of carbon fluxes in the Amazon basin? A data-model intercomparison. *Glob. Change Biol.* **23**, 191–208 (2017).
44. Xu, L. et al. Satellite observation of tropical forest seasonality: spatial patterns of carbon exchange in Amazonia. *Environ. Res. Lett.* **10**, 084005 (2015).
45. Wu, J. et al. Biological processes dominate seasonality of remotely sensed canopy greenness in an Amazon evergreen forest. *New Phytol.* **217**, 1507–1520 (2018).
46. Piao, S. et al. Characteristics, drivers and feedbacks of global greening. *Nat. Rev. Earth Environ.* **1**, 14–27 (2019).
47. Chen, X. et al. Vapor pressure deficit and sunlight explain seasonality of leaf phenology and photosynthesis across Amazonian evergreen broadleaved forest. *Glob. Biogeochem. Cycles* **35**, e2020GB006893 (2021).
48. Santos De Lima, L. et al. Severe droughts reduce river navigability and isolate communities in the Brazilian Amazon. *Commun. Earth Environ.* **5**, 370 (2024).
49. Santos, V. A. H. F. dos et al. Causes of reduced leaf-level photosynthesis during strong El Niño drought in a Central Amazon forest. *Glob. Change Biol.* **24**, 4266–4279 (2018).
50. Green, J. K. et al. Amazon rainforest photosynthesis increases in response to atmospheric dryness. *Sci. Adv.* **6**, eabb7232 (2020).
51. Wright, I. J. et al. The worldwide leaf economics spectrum. *Nature* **428**, 821–827 (2004).
52. Kono, Y. et al. Initial hydraulic failure followed by late-stage carbon starvation leads to drought-induced death in the tree *Trema orientalis*. *Commun. Biol.* **2**, 8 (2019).
53. Fan, Y. et al. Hydrologic regulation of plant rooting depth. *Proc. Natl Acad. Sci. USA* **114**, 10572–10577 (2017).
54. Tao, S. et al. Increasing and widespread vulnerability of intact tropical rainforests to repeated droughts. *Proc. Natl Acad. Sci. USA* **119**, e2116626119 (2022).
55. Hansen, M. C. et al. High-resolution global maps of 21st-century forest cover change. *Science* **342**, 850–853 (2013).
56. Su, Y. et al. Asymmetric influence of forest cover gain and loss on land surface temperature. *Nat. Clim. Change* **13**, 823–831 (2023).
57. Chuvieco, E. et al. ESA Fire Climate Change Initiative (Fire_cci): MODIS Fire_cci Burned Area Pixel product, version 5.1. *Centre for Environmental Data Analysis* https://doi.org/10.5285/58f00d8814064b79a0c49662ad3af537 (2018).
58. Vancutsem, C. et al. Long-term (1990–2019) monitoring of forest cover changes in the humid tropics. *Sci. Adv.* **7**, eabe1603 (2021).
59. Gyimah, R. & Nakao, T. Early growth and photosynthetic responses to light in seedlings of three tropical species differing in successional strategies. *New For.* **33**, 217–236 (2007).

60. Farquhar, G. D., Von Caemmerer, S. & Berry, J. A. A biochemical model of photosynthetic CO_2 assimilation in leaves of C_3 species. *Planta* **149**, 78–90 (1980).
61. Chen, J. M. et al. Daily canopy photosynthesis model through temporal and spatial scaling for remote sensing applications. *Ecol. Model.* **124**, 99–119 (1999).
62. Chen, J. M. et al. Vegetation structural change since 1981 significantly enhanced the terrestrial carbon sink. *Nat. Commun.* **10**, 4259 (2019).
63. Stocker, B. D. et al. P-model v1.0: an optimality-based light use efficiency model for simulating ecosystem gross primary production. *Geosci. Model Dev.* **13**, 1545–1581 (2020).
64. Fisher, R. A. et al. Taking off the training wheels: the properties of a dynamic vegetation model without climate envelopes, CLM4.5(ED). *Geosci. Model Dev.* **8**, 3593–3619 (2015).
65. Chen, J. M. et al. Leaf area index measurements at Fluxnet–Canada forest sites. *Agric. For. Meteorol.* **140**, 257–268 (2006).
66. Wang, R. et al. Seasonality of leaf area index and photosynthetic capacity for better estimation of carbon and water fluxes in evergreen conifer forests. *Agric. For. Meteorol.* **279**, 107708 (2019).
67. Yang, X. et al. A gridded dataset of a leaf-age-dependent leaf area index seasonality product over tropical and subtropical evergreen broadleaved forests. *Earth Syst. Sci. Data* **15**, 2601–2622 (2023).
68. Medlyn, B. E. et al. Reconciling the optimal and empirical approaches to modelling stomatal conductance: reconciling optimal and empirical stomatal models. *Glob. Change Biol.* **17**, 2134–2144 (2011).
69. Bernacchi, C. J. et al. Modelling C_3 photosynthesis from the chloroplast to the ecosystem. *Plant Cell Environ.* **36**, 1641–1657 (2013).
70. Zhao, K., Popescu, S. & Nelson, R. Lidar remote sensing of forest biomass: a scale-invariant estimation approach using airborne lasers. *Remote Sens. Environ.* **113**, 182–196 (2009).
71. Chavana-Bryant, C. et al. Leaf aging of Amazonian canopy trees as revealed by spectral and physiochemical measurements. *New Phytol.* **214**, 1049–1063 (2017).
72. Seyednasrollah, B. et al. Publisher correction: tracking vegetation phenology across diverse biomes using version 2.0 of the PhenoCam dataset. *Sci. Data* **6**, 261 (2019).
73. Derived monthly leaf demography for the 134 vine-free upper canopy tree crowns that exhibited at least two leaf flush events during Jul2013–Nov2018. *ATTO* https://doi.org/10.17871/ATTO.230.4.842 (2025).
74. Coley, P. D. Herbivory and defensive characteristics of tree species in a lowland tropical forest. *Ecol. Monogr.* **53**, 209–229 (1983).
75. Reich, P. B. et al. Leaf lifespan as a determinant of leaf structure and function among 23 amazonian tree species. *Oecologia* **86**, 16–24 (1991).
76. Reich, P. B. et al. Generality of leaf trait relationships: a test across six biomes. *Ecology* **80**, 1955–1969 (1999).
77. Lugo, A. E. Comparison of tropical tree plantations with secondary forests of similar age. *Ecol. Monogr.* **62**, 2–41 (1992).
78. Santiago, L. S. & Wright, S. J. Leaf functional traits of tropical forest plants in telation to growth form. *Funct. Ecol.* **21**, 19–27 (2007).
79. Chave, J. et al. Above-ground biomass and productivity in a rain forest of eastern South America. *J. Trop. Ecol.* **24**, 355–366 (2008).
80. Kattge, J. et al. TRY plant trait database—enhanced coverage and open access. *Glob. Change Biol.* **26**, 119–188 (2020).
81. Wang, F. et al. Contrasting age-dependent leaf acclimation strategies drive vegetation greening across deciduous broadleaf forests in mid- to high latitudes. *Nat. Plants* **11**, 1748–1758 (2025).
82. Janssen, T. et al. Drought effects on leaf fall, leaf flushing and stem growth in the Amazon forest: reconciling remote sensing data and field observations. *Biogeosciences* **18**, 4445–4472 (2021).
83. Zhang, H. et al. Accurate representation of leaf longevity is important for simulating ecosystem carbon cycle. *Basic Appl. Ecol.* **17**, 396–407 (2016).
84. Bradley, A. V. et al. Relationships between phenology, radiation and precipitation in the Amazon region. *Glob. Change Biol.* **17**, 2245–2260 (2011).
85. Gloor, M. et al. Recent Amazon climate as background for possible ongoing and future changes of Amazon humid forests. *Glob. Biogeochem. Cycles* **29**, 1384–1399 (2015).
86. Meyer, H. et al. Improving performance of spatio-temporal machine learning models using forward feature selection and target-oriented validation. *Environ. Model. Softw.* **101**, 1–9 (2018).
87. Ploton, P. et al. Spatial validation reveals poor predictive performance of large-scale ecological mapping models. *Nat. Commun.* **11**, 4540 (2020).
88. Hollunder, R. K. et al. Vapor pressure deficit drives the mortality of understorey woody plants during drought recovery in the Atlantic forest. *J. Veg. Sci.* **35**, e13222 (2024).
89. McDowell, N. et al. Drivers and mechanisms of tree mortality in moist tropical forests. *New Phytol.* **219**, 851–869 (2023).
90. Esquivel-Muelbert, A. et al. Tree mode of death and mortality risk factors across Amazon forests. *Nat. Commun.* **11**, 5515 (2020).
91. Breiman, L. Random forests. *Mach. Learn.* **45**, 5–32 (2001).
92. Friedman, J. H. Greedy function approximation: a gradient boosting machine. *Ann. Stat.* **29**, 1189–1232 (2001).
93. Su, Y. et al. Pervasive but biome-dependent relationship between fragmentation and resilience in forests. *Nat. Ecol. Evol.* **9**, 1670–1684 (2025).
94. Ziehn, T. et al. The Australian Earth System Model: ACCESS-ESM1.5. *J. South. Hemisph. Earth Syst. Sci.* **70**, 193–214 (2020).
95. Swart, N. C. et al. CCCma CanESM5 model output prepared for CMIP6 ScenarioMIP. *Earth System Grid Federation* https://doi.org/10.22033/ESGF/CMIP6.1317 (2019).
96. Lovato, T., Peano, D. & Butenschön, M. CMCC CMCC-ESM2 model output prepared for CMIP6 ScenarioMIP. *Earth System Grid Federation* https://doi.org/10.22033/ESGF/CMIP6.13168 (2021).
97. Voldoire, A. CNRM-CERFACS CNRM-CM6-1 model output prepared for CMIP6 ScenarioMIP. *Earth System Grid Federation* https://doi.org/10.22033/ESGF/CMIP6.1384 (2019).
98. Voldoire, A. CNRM-CERFACS CNRM-CM6-1-HR model output prepared for CMIP6 ScenarioMIP. *Earth System Grid Federation* https://doi.org/10.22033/ESGF/CMIP6.1388 (2019).
99. Seferian, R. CNRM-CERFACS CNRM-ESM2-1 model output prepared for CMIP6 ScenarioMIP. *Earth System Grid Federation* https://doi.org/10.22033/ESGF/CMIP6.1395 (2019).
100. Dunne, J. P. et al. The GFDL Earth System Model Version 4.1 (GFDL-ESM 4.1): overall coupled model description and simulation characteristics. *J. Adv. Model. Earth Syst.* **12**, e2019MS002015 (2020).
101. NASA Goddard Institute for Space Studies (NASA/GISS). IPCC DDC: NASA-GISS GISS-E2.1G model output prepared for CMIP6 ScenarioMIP. *World Data Center for Climate (WDCC) at DKRZ* https://doi.org/10.26050/WDCC/AR6.C6SPGIGEG (2023).
102. Volodin, E. et al. IPCC DDC: INM INM-CM4-8 model output prepared for CMIP6 ScenarioMIP. *World Data Center for Climate (WDCC) at DKRZ* https://doi.org/10.26050/WDCC/AR6.C6SPINIC8 (2023).
103. Volodin, E. et al. IPCC DDC: INM INM-CM5-0 model output prepared for CMIP6 ScenarioMIP. *World Data Center for Climate (WDCC) at DKRZ* https://doi.org/10.26050/WDCC/AR6.C6SPINIC0 (2023).

104. Boucher, O. et al. IPCC DDC: IPSL IPSL-CM6A-LR model output prepared for CMIP6 ScenarioMIP. *World Data Center for Climate (WDCC) at DKRZ* https://doi.org/10.26050/WDCC/AR6.C6SPIPICL (2023).
105. Tachiiri, K. et al. IPCC DDC: MIROC MIROC-ES2L model output prepared for CMIP6 ScenarioMIP. *World Data Center for Climate (WDCC) at DKRZ* https://doi.org/10.26050/WDCC/AR6.C6SPMIMIL (2023).
106. Schupfner, M. et al. IPCC DDC: DKRZ MPI-ESM1.2-HR model output prepared for CMIP6 ScenarioMIP. *World Data Center for Climate (WDCC) at DKRZ* https://doi.org/10.26050/WDCC/AR6.C6SPDKME2 (2023).
107. Yukimoto, S. et al. IPCC DDC: MRI MRI-ESM2.0 model output prepared for CMIP6 ScenarioMIP. *World Data Center for Climate (WDCC) at DKRZ* https://doi.org/10.26050/WDCC/AR6.C6SPMRME0 (2023).
108. Good, P. et al. IPCC DDC: MOHC UKESM1.0-LL model output prepared for CMIP6 ScenarioMIP. *World Data Center for Climate (WDCC) at DKRZ* https://doi.org/10.26050/WDCC/AR6.C6SPMOU0 (2023).
109. Lange, S. Trend-preserving bias adjustment and statistical downscaling with ISIMIP3BASD (v1. 0). *Geosci. Model Dev.* **12**, 3055–3070 (2019).
110. Lange, S. ISIMIP3BASD (version 2.4.1). *Zenodo* https://doi.org/10.5281/zenodo.3898426 (2021).
111. Wenger, S. J. & Olden, J. D. Assessing transferability of ecological models: an underappreciated aspect of statistical validation. *Methods Ecol. Evol.* **3**, 260–267 (2012).
112. Xueqin, Y. & Xiuzhi, C. High-resolution leaf age-dependent LAI time-series dataset across Amazon rainforests *Zenodo* https://zenodo.org/records/18271110 (2025).
113. Yang, X. et al. Code to support 'Amazon rainforests are rejuvenating their canopies by producing more photosynthetically efficient young leaves under climate change'. *Zenodo* https://doi.org/10.5281/zenodo.18269018 (2026).
114. Malhi, Y. et al. Exploring the likelihood and mechanism of a climate-change-induced dieback of the Amazon rainforest. *Proc. Natl Acad. Sci. USA* **106**, 20610–20615 (2009).
115. Xu, X. et al. Climate regime shift and forest loss amplify fire in Amazonian forests. *Glob. Change Biol.* **26**, 5874–5885 (2020).
116. Tang, H. & Dubayah, R. Light-driven growth in Amazon evergreen forests explained by seasonal variations of vertical canopy structure. *Proc. Natl Acad. Sci. USA* **114**, 2640–2644 (2017).

Acknowledgements

We thank S. J. Wright from the Smithsonian Tropical Research Institute, T. F. Domingues from University of São Paulo and D. R. Rossatto from São Paulo State University for the constructive comments or short communications or valuable help for contacting potential colleagues through email. We thank S. Botía, G. Martins, D. Pinho and A. Pontes-Lopes for construction of the Central Amazon leaf demography dataset derived from the ATTO PhenoCam. This study was supported by the National Natural Science Foundation of China (grant nos. 42471326, 31971458 and U21A6001), the National Key R&D Program of China (grant no. 2024YFF1306600) and the Science and Technology Program of Guangdong (grant no. 2024B1212070012). P.B.R. was supported by the National Science Foundation: Biological Integration Institutes NSF-DBI-2021898. J. Wu was supported by the Innovation and Technology Fund (Funding Support to State Key Laboratory of Agrobiotechnology).

Author contributions

X.C. designed the study and wrote the initial paper and revised the paper. X.Y. and J.T. collected the data, performed the analysis, drew the figures and wrote Methods section. P.C., L.Z., P.B.R., J. Wu, J.S., J.C., J. Lamour, I.M., Y.H.F., J.M.C., J. Liu, S.T., X. Xiao, X. Xu, Y.S., H.Z., Z.Z., Y.Z., D.H., L.C., Q.L., R.L., K. Yan, P.L., X.L., P.M., H.L., D.B., B.W.N., H.T., J. Wang, K. Yu, W.Y. and S.W. contributed to discussing the scientific question and revising the paper.

Competing interests

The authors declare no competing interests.

Additional information

Supplementary information The online version contains supplementary material available at https://doi.org/10.1038/s41477-026-02240-9.

Correspondence and requests for materials should be addressed to Xiuzhi Chen.

Peer review information *Nature Plants* thanks Cecilia Chavana-Bryant, Gabriel B. Costa and Qin Ma for their contribution to the peer review of this work.

Reprints and permissions information is available at www.nature.com/reprints.

---

[1]Guangdong Province Data Center of Terrestrial and Marine Ecosystems Carbon Cycle, School of Atmospheric Sciences, School of Ecology, Sun Yat-sen University, Zhuhai, China. [2]Laboratoire des Sciences du Climat et de l'Environnement, Université Paris-Saclay, IPSL, CEA-CNRS-UVSQ, if sur Yvette, France. [3]Department of Atmospheric and Environmental Sciences, State University of New York at Albany, Albany, NY, USA. [4]Institute for Global Change Biology and School for Environment and Sustainability, University of Michigan, Ann Arbor, MI, USA. [5]Department of Forest Resources, University of Minnesota, St. Paul, MN, USA. [6]School of Biological Sciences and Institute for Climate and Carbon Neutrality, The University of Hong Kong, Hong Kong, China. [7]State Key Laboratory of Agrobiotechnology (CUHK), Hong Kong, China. [8]Ottawa Research and Development Centre, Agriculture and Agri-Food Canada, Ottawa, Ontario, Canada. [9]Centre de Recherche sur la Biodiversite et l'Environnement (CRBE), Universite de Toulouse, CNRS, IRD, Toulouse INP, Toulouse, France. [10]AMAP, Université Montpellier, INRAE, CIRAD, CNRS, IRD, Montpellier, France. [11]College of Water Sciences, Beijing Normal University, Beijing, China. [12]Department of Geography and Planning, University of Toronto, Toronto, Ontario, Canada. [13]Institute of Ecology, College of Urban and Environmental Sciences, Peking University, Beijing, China. [14]School of Biological Sciences, University of Oklahoma, Norman, OK, USA. [15]Department of Ecology and Evolutionary Biology, Cornell University, Ithaca, NY, USA. [16]State Key Laboratory of Urban and Regional Ecology, Research Center for Eco-Environmental Sciences, Chinese Academy of Sciences, Beijing, China. [17]School of Geography and Planning, Sun Yat-sen University, Guangzhou, China. [18]School of Urban Planning and Design, Peking University, Shenzhen, China. [19]Institute of Carbon Neutrality, College of Urban and Environmental Sciences, Peking University, Beijing, China. [20]Atmospheric, Climate, & Earth Sciences Division, Pacific Northwest National Laboratory, Richland, WA, USA.

[21]Key Laboratory of Bio-Resource and Eco-Environment of Ministry of Education, College of Life Sciences, Sichuan University, Chengdu, China. [22]State Key Laboratory of Climate System Prediction and Risk Management, Nanjing University of Information Science and Technology, Nanjing, China. [23]School of Remote Sensing and Geomatics Engineering, Nanjing University of Information Science and Technology, Nanjing, China. [24]Department of Agricultural and Environmental Sciences, University of Bari 'A. Moro', Bari, Italy. [25]State Key Laboratory of Remote Sensing and Digital Earth, Advanced Interdisciplinary Institute of Satellite Applications, Faculty of Geographical Science, Beijing Normal University, Beijing, China. [26]School of Geographic Sciences, Hunan Normal University, Changsha, China. [27]School of GeoSciences, University of Edinburgh, Edinburgh, UK. [28]South China Botanical Garden, Chinese Academy of Sciences, Guangzhou, China. [29]Université de Lorraine, INRAE, UMR Silva, AgroParisTech, Nancy, France. [30]Environmental Dynamics Department, National Institute for Amazon Research, Manaus, Brazil. [31]Department of Geography, National University of Singapore, Singapore, Singapore. [32]Institute of Geographical Sciences and Natural Resources Research, Chinese Academy of Sciences, Beijing, China. [33]Department of Land Surveying and Geo-Informatics, The Hong Kong Polytechnic University, Hong Kong, China. [34]These authors contributed equally: Xueqin Yang, Jie Tian.
✉e-mail: chenxzh73@mail.sysu.edu.cn

nature portfolio

Corresponding author(s): xiuzhi chen

Last updated by author(s): Jan 16, 2026

Reporting Summary

Nature Portfolio wishes to improve the reproducibility of the work that we publish. This form provides structure for consistency and transparency in reporting. For further information on Nature Portfolio policies, see our Editorial Policies and the Editorial Policy Checklist.

Statistics

For all statistical analyses, confirm that the following items are present in the figure legend, table legend, main text, or Methods section.

n/a	Confirmed	
☐	☒	The exact sample size (*n*) for each experimental group/condition, given as a discrete number and unit of measurement
☐	☒	A statement on whether measurements were taken from distinct samples or whether the same sample was measured repeatedly
☐	☒	The statistical test(s) used AND whether they are one- or two-sided *Only common tests should be described solely by name; describe more complex techniques in the Methods section.*
☐	☒	A description of all covariates tested
☐	☒	A description of any assumptions or corrections, such as tests of normality and adjustment for multiple comparisons
☐	☒	A full description of the statistical parameters including central tendency (e.g. means) or other basic estimates (e.g. regression coefficient) AND variation (e.g. standard deviation) or associated estimates of uncertainty (e.g. confidence intervals)
☐	☒	For null hypothesis testing, the test statistic (e.g. F, t, r) with confidence intervals, effect sizes, degrees of freedom and P value noted *Give P values as exact values whenever suitable.*
☐	☒	For Bayesian analysis, information on the choice of priors and Markov chain Monte Carlo settings
☐	☒	For hierarchical and complex designs, identification of the appropriate level for tests and full reporting of outcomes
☐	☒	Estimates of effect sizes (e.g. Cohen's d, Pearson's r), indicating how they were calculated

Our web collection on statistics for biologists contains articles on many of the points above.

Software and code

Policy information about availability of computer code

Data collection	The softwares for coding are Python 3.10 and Matlab r2019b.
Data analysis	The codes used for data analysis are available at website: https://doi.org/10.5281/zenodo.18269018

For manuscripts utilizing custom algorithms or software that are central to the research but not yet described in published literature, software must be made available to editors and reviewers. We strongly encourage code deposition in a community repository (e.g. GitHub). See the Nature Portfolio guidelines for submitting code & software for further information.

Data

Policy information about availability of data

All manuscripts must include a data availability statement. This statement should provide the following information, where applicable:

- Accession codes, unique identifiers, or web links for publicly available datasets
- A description of any restrictions on data availability
- For clinical datasets or third party data, please ensure that the statement adheres to our policy

All the original datasets used in this research are publicly available from their sources, LAI-age cohort product: https://doi.org/10.5281/zenodo.18271110; PML-V2 GPP datasets: https://developers.google.com/earth-engine/datasets/catalog/CAS_IGSNRR_PML_V2_v018#description; Terraclimate Tmin, Tmax, Pre, VPD, SW, PET, AET, PDSI: https://www.climatologylab.org/terraclimate.html; ERA5-Land SM: https://cds.climate.copernicus.eu/cdsapp#!/dataset/reanalysis-era5-land-monthly-means?tab=overview; Global canopy height map for 2020 (hc): https://doi.org/10.3929/ethz-b-000609802; Global elevation: https://www.eorc.jaxa.jp/ALOS/en/

dataset/aw3d30/aw3d30_e.htm; CMIP6 models variable: https://aims2.llnl.gov/search/?project=CMIP6/; ISIMIP models: https://www.isimip.org/outputdata/?simulation_round=ISIMIP3b; MCD12Q1 v061 landcover: https://www.earthdata.nasa.gov/data/catalog/lpcloud-mcd12q1-061; Global Land Cover and Land Use Change, 2000-2020: https://glad.umd.edu/dataset/GLCLUC2020/; ESA CCI Fire v5.1: https://dx.doi.org/10.5285/58f00d8814064b79a0c49662ad3af537; SPEI : https://doi.org/10.5285/ac43da11867243a1bb414e1637802dec; Tropical moist forests product: https://forobs.jrc.ec.europa.eu/TMF/; Camera-based time-series and seasonal LAI age cohort data: https://phenocam.nau.edu/webcam/ and https://doi.org/10.17871/ATTO.230.4.842; In situ leaf turnover rate observation data: https://doi.org/10.1016/j.baae.2016.01.006; Field LMA datasets in Plant Trait Database (TRY): https://www.try-db.org/TryWeb/Home.php

Research involving human participants, their data, or biological material

Policy information about studies with human participants or human data. See also policy information about sex, gender (identity/presentation), and sexual orientation and race, ethnicity and racism.

Reporting on sex and gender	This study does not involve any relative context.
Reporting on race, ethnicity, or other socially relevant groupings	This study does not involve any relative context.
Population characteristics	This study does not involve any relative context.
Recruitment	This study does not involve any relative context.
Ethics oversight	This study does not involve any relative context.

Note that full information on the approval of the study protocol must also be provided in the manuscript.

Field-specific reporting

Please select the one below that is the best fit for your research. If you are not sure, read the appropriate sections before making your selection.

☐ Life sciences ☐ Behavioural & social sciences ☒ Ecological, evolutionary & environmental sciences

For a reference copy of the document with all sections, see nature.com/documents/nr-reporting-summary-flat.pdf

Ecological, evolutionary & environmental sciences study design

All studies must disclose on these points even when the disclosure is negative.

Study description	Leaf age structure strongly regulates canopy photosynthesis in Amazon rainforests, yet its large-scale patterns and dynamics remain poorly understood. Here we map the fraction of leaf area of photosynthetically efficient young leaves (fyoung) using remote sensing data and assess its spatiotemporal variability from 2001 to 2023. We find that fyoung varies markedly with elevation and canopy height: tall mountain forests (canopy ≥ 32 m or elevation ≥ 300 m) exhibit higher fyoung than short lowland forests, reflecting higher leaf turnover driven by stronger radiation, greater atmospheric dryness, and longer dry seasons. Across the basin, fyoung increased significantly in 85.2% of forests during 2001-2023, linked to decreasing precipitation, rising sunlight, intensifying atmospheric dryness, and lengthening dry seasons. This widespread trend towards more juvenile leaves is projected to persist under future climate change. Our findings reveal a fundamental shift in Amazon leaf age structure and highlight its importance for predicting future photosynthetic responses in a warmer, drier climate.
Research sample	We produced 1km resolution maps of the fraction of leaf area of photosynthetically efficient young leaves (fyoung) using remote sensing data and assess its spatiotemporal variability from 2001 to 2023. In total, we collected camera-based images from eight Amazonian sites to develop the field dataset of LAInew, LAIyoung and LAIold (Fig. S2a; Supplementary Dataset 4). Data for the K67 and K34 flux tower sites were derived from Ref.1. For the remaining six sites, we used the classification procedure described above to compute the LAInew, LAIyoung and LAIold. The camera-based canopy photos at Barro Colorado (March 2013 to December 2023), Barro Colorado2 (November 2014 to September 2015), Elverde (November 2014 to December 2020), NEON GUAN (December 2016 to September 2018) and Soltis (July 2018 to April 2022) sites were obtained from the website75: https://phenocam.nau.edu/webcam/ (last access: 2 Oct. 2025). The data from the ATTO (July 2013 to November 2018) site were provided at15: https://doi.org/10.17871/ATTO.230.4.842 (last access: 2 Oct. 2025). The satellite-derived fyoung, calculated as the fraction of LAIyoung to LAItotal, was verified against three datasets: 10 annul mean leaf lifespan measured at 5 field sites (triangle symbols), 331 leaf lifespan estimates derived from 193 in-situ leaf mass per area (LMA) records collected at 148 sites (circle symbols), and 138 litterfall seasonality records from 66 sites (square symbols) (Fig. S3a; Supplementary Dataset 5-7).
Sampling strategy	Collect all the data over tropical region. To remove the impacts of natural and anthropogenic disturbances, we excluded all grid cells affected by recent fires and changes in forest cover (e.g., afforestation and deforestation), as well as degradation. We focused exclusively on intact Amazon rainforests, where forest cover exceeds 90%.
Data collection	All the original datasets used in this research are publicly available from their sources, LAI-age cohort product: https://doi.org/10.5281/zenodo.18271110; PML-V2 GPP datasets: https://developers.google.com/earth-engine/datasets/catalog/CAS_IGSNRR_PML_V2_v018#description; Terraclimate Tmin, Tmax, Pre, VPD, SW, PET, AET, PDSI: https://www.climatologylab.org/terraclimate.html; ERA5-Land SM: https://cds.climate.copernicus.eu/cdsapp#!/dataset/reanalysis-era5-land-monthly-means?tab=overview; Global canopy height map for 2020 (hc): https://doi.org/10.3929/ethz-b-000609802; Global elevation: https://

www.eorc.jaxa.jp/ALOS/en/dataset/aw3d30/aw3d30_e.htm; CMIP6 models variable: https://aims2.llnl.gov/search/?project=CMIP6/; ISIMIP models: https://www.isimip.org/outputdata/?simulation_round=ISIMIP3b; MCD12Q1 v061 landcover: https://www.earthdata.nasa.gov/data/catalog/lpcloud-mcd12q1-061; Global Land Cover and Land Use Change, 2000-2020: https://glad.umd.edu/dataset/GLCLUC2020/; ESA CCI Fire v5.1: https://dx.doi.org/10.5285/58f00d8814064b79a0c49662ad3af537; SPEI : https://doi.org/10.5285/ac43da11867243a1bb414e1637802dec; Tropical moist forests product: https://forobs.jrc.ec.europa.eu/TMF/; Camera-based time-series and seasonal LAI age cohort data: https://phenocam.nau.edu/webcam/ and https://doi.org/10.17871/ATTO.230.4.842; In situ leaf turnover rate observation data: https://doi.org/10.1016/j.baae.2016.01.006; Field LMA datasets in Plant Trait Database (TRY): https://www.try-db.org/TryWeb/Home.php

Timing and spatial scale

time period: 2001-2023
spatial scale: over the Amazon rainforests

Data exclusions

In this study, we focused exclusively on the areas in American tropical rainforests (ATRs) (18°N~18°S) that were not affected by anthropogenic and natural disturbances between 2001 and 2023. First, we identified the grid cells (1-km resolution) classified as “evergreen broadleaf forests” using MODIS land cover imagery (MCD12Q1). We specifically targeted the intact ATRs with a forest cover exceeding 90%. Subsequently, these areas were resampled to a 1-km resolution for further analysis. Next, we overlaid the 30-m resolution global tree cover change maps obtained from the Global Forest Watch (GFW) with the 1-km resolution MODIS land cover maps. We excluded the 1-km resolution forest grid cells that ever experienced either forest gains (fraction > 0.02) or losses (fraction > 0.02) from 2001 to 2020, following the methodology outlined by Su et al. (2023). To minimize wildfire impacts, we excluded grid cells containing burned areas throughout the study period. The gridded dataset depicting forest burned areas was derived from the MODIS Fire_cci Burned Area Pixel Product (Version 5.1), at a spatial resolution of 1-km and a monthly temporal resolution. Detection of degraded areas was based on the TMF forest cover change data.

To exclude the impacts of severe drought events, we implemented an integrated drought assessment framework. This framework integrated the Palmer Drought Severity Index (PDSI), the Standardized Precipitation Evapotranspiration Index (SPEI), and Cumulative Water Deficit (CWD). A grid cell was considered to be experiencing severe drought when the annual anomalies from any indices (PDSI, SPEI, and CWD) for a given year fell one standard deviation below the mean of the 2001-2023 time-series. We then used the differences in fyoung seasonality between unusual and normal dry seasons to represent the impacts of unusual dry seasons (i.e., severe drought) on fyoung. For time-series analysis, forest grid cells experiencing severe droughts for more than nine years were excluded from the analysis. Otherwise, forest gird cells were retained, but data from years coinciding with severe droughts were removed.

Reproducibility

Optical satellite signals tend to saturate in dense canopies so that the spatial and temporal variations in the total LAI of ATRs are poorly represented by satellite sensors. Thus, we selected the valid MODIS LAI (collection 6) data for each pixel across ATRs following the method developed by Samanta et al. (2012). The value of valid MODIS LAI for each pixel was defined as the sum of LAIclass1, LAIclass2, and LAIclass3 in Equation 1. Grid cells were considered valid when (a) data were of good quality, with “SCF_QC” equaling 0 (main algorithm without saturation) or 1 (main algorithm with saturation), (b) Clouds were absent, as indicated by “CloudState” (0), “Cirrus” (0), “Internal_CloudMask” (0), and “Cloud_Shadow” (0). The validity of the selected grid cells was further examined by using the MOD13A1 cloud and aerosol flags, following the methodology outlined by Samanta et al. (2012).

This invariant seasonality of total LAI has also been integrated into the LSMs to successfully simulate both site-level and regional-scale photosynthesis, as well as the litterfall seasonality across the Amazon region. To assess the temporal changes in total LAI, we collected the time-series LAI data from four field observation sites across ATRs, all indicating marginally small inter-annual changes. Additionally, based on these valid grid cells, analysis also revealed no significant change (P = 0.18) in total LAI over ATRs from the 2001 to 2023 period.

Randomization

We focused on the grid cells without any disturbances. So, we used all the data of those un-disturbanced pixels.

Blinding

This study does not involve any relative context.

Did the study involve field work? ☒ Yes ☐ No

Field work, collection and transport

Field conditions

In total, we collected camera-based images from eight Amazonian sites to develop the field dataset of LAInew, LAIyoung and LAIold (Fig. S2a; Supplementary Dataset 4). Data for the K67 and K34 flux tower sites were derived from Ref.1. For the remaining six sites, we used the classification procedure described above to compute the LAInew, LAIyoung and LAIold. The camera-based canopy photos at Barro Colorado (March 2013 to December 2023), Barro Colorado2 (November 2014 to September 2015), Elverde (November 2014 to December 2020), NEON GUAN (December 2016 to September 2018) and Soltis (July 2018 to April 2022) sites were obtained from the website75: https://phenocam.nau.edu/webcam/ (last access: 2 Oct. 2025). The data from the ATTO (July 2013 to November 2018) site were provided at15: https://doi.org/10.17871/ATTO.230.4.842 (last access: 2 Oct. 2025). The satellite-derived fyoung, calculated as the fraction of LAIyoung to LAItotal, was verified against three datasets: 10 annul mean leaf lifespan measured at 5 field sites (triangle symbols), 331 leaf lifespan estimates derived from 193 in-situ leaf mass per area (LMA) records collected at 148 sites (circle symbols), and 138 litterfall seasonality records from 66 sites (square symbols) (Fig. S3a; Supplementary Dataset 5-7).

Location

Over Amazon rainforests

Access & import/export

We collected all the field data published online. These field data can be available and used freely.

Disturbance

This study does not involve any relative context.

Reporting for specific materials, systems and methods

We require information from authors about some types of materials, experimental systems and methods used in many studies. Here, indicate whether each material, system or method listed is relevant to your study. If you are not sure if a list item applies to your research, read the appropriate section before selecting a response.

Materials & experimental systems

n/a	Involved in the study	
☒	☐	Antibodies
☒	☐	Eukaryotic cell lines
☒	☐	Palaeontology and archaeology
☒	☐	Animals and other organisms
☒	☐	Clinical data
☒	☐	Dual use research of concern
☒	☐	Plants

Methods

n/a	Involved in the study	
☒	☐	ChIP-seq
☒	☐	Flow cytometry
☒	☐	MRI-based neuroimaging

Plants

Seed stocks	This study does not involve any relative context.
Novel plant genotypes	This study does not involve any relative context.
Authentication	This study does not involve any relative context.